Atmos. Chem. Phys. Discuss., 9, 23589–23622, 2009
www.atmos-chem-phys-discuss.net/9/23589/2009/

Atmospheric Chemistry and Physics Discussions

This discussion paper is/has been under review for the journal Atmospheric Chemistry and Physics (ACP). Please refer to the corresponding final paper in ACP if available.

On the transitions in marine boundary layer cloudiness

I. Sandu[1], **B. Stevens**[1,2], **and R. Pincus**[3]

[1]Max Planck Institute for Meteorology, Hamburg, Germany
[2]University of California at Los Angeles, Los Angeles, California, USA
[3]University of Colorado/NOAA Earth System Research Lab, Boulder, Colorado, USA

Received: 2 October 2009 – Accepted: 27 October 2009 – Published: 5 November 2009

Correspondence to: I. Sandu (irina.sandu@zmaw.de)

Published by Copernicus Publications on behalf of the European Geosciences Union.

Abstract

Satellite observations and meteorological reanalysis are used to examine the transition from unbroken sheets of stratocumulus to fields of scattered cumulus, and the processes controlling them, in four subtropical ocean basins. A Lagrangian analysis suggests that both the transition, defined as the temporal evolution in cloudiness, and the processes driving the transition, are quite similar among the oceanic basins. The transitions in marine boundary layer cloudiness are an extremely persistent feature of the subtropical ocean's environment, so that the transitions' characteristics obtained by documenting the flow of thousands of individual air masses are well reproduced by the mean (or climatological) fields of the different data sets. This opens new opportunities for future observations and modeling studies of these transitions.

1 Introduction

A striking feature of the global cloud climatology is the transition from unbroken sheets of stratocumulus to fields of scattered cumulus that occurs as boundary-layer air masses advect equatorward in the trades (Von Ficker, 1936; McDonald, 1938; Neiburger et al., 1961; Malkus and Riehl, 1964; Klein and Hartmann, 1993). In the eastern basins of the subtropical oceans, the regions adjacent to the continental coasts are frequently covered by extensive sheets of stratocumulus. These stratocumulus sheets form over relatively cold sea-surface temperatures (SSTs), in shallow and generally well-mixed boundary layers capped by a strong temperature inversion. As the air masses advect equatorward over warmer SSTs and towards lower mean large-scale subsidence, the inversion generally weakens and rises and the stratocumulus decks break-up. Ultimately, the stratocumulus is replaced by scattered, predominantly shallow cumulus. The shift, or transition in cloud regimes has a profound effect on the local albedo, and begs explanation, particularly by those interested in understanding the factors controlling the planetary albedo as a whole.

ACPD

9, 23589–23622, 2009

Early studies of the stratocumulus to cumulus transition followed the equatorward advection of a cloudy air column and documented its evolution either in situ (Albrecht et al., 1995; Bretherton and Pincus, 1995; De Roode and Duynkerke, 1997), or from satellite data and operational weather analysis (Pincus et al., 1997). Such a Lagrangian perspective on the cloud evolution naturally accounts for both the time-varying boundary conditions experienced by the air mass during its equatorward advection and the time-scale on which the boundary layer clouds adjust to such environmental changes (Schubert et al., 1979; Klein and Norris, 1995; Pincus et al., 1997). The structure of the transition documented by these observational studies was further explored with mixed-layer models and two-dimensional fine-scale numerical simulations (Bretherton, 1992; Bretherton and Wyant, 1997; Bretherton et al., 1999; Krueger et al., 1995; Wyant et al., 1997; Stevens, 2000). This work led to the development of a simple conceptual model of the transition. According to this model, the cloud breakup is fundamentally driven by increasing SSTs. Convective activity driven by the surface latent heat fluxes increases as the air advects over warmer waters. The strengthening of convectively driven turbulence enhances the entrainment of warm and dry free-tropospheric air at cloud top, which leads to a differentiation (stabilization) of the cloud with respect to the subcloud layer. This differentiation inhibits the transport of moisture towards the cloud layer. Consequently, the subcloud layer frequently becomes conditionally unstable, and cumulus clouds develop at its top. Meanwhile, the stratocumulus gradually thins and evaporates due to increased entrainment at cloud top and reduced moisture supply from the surface. Finally, it dissipates into thin and broken patches, penetrated from below by cumulus clouds.

These ideas about the transitions in marine boundary layer cloudiness rely on a handful of case studies drawn exclusively from the transition regions of the Northern Hemisphere. Here we seek to understand the extent to which the transition, and the processes governing it, are similar (or not) in all the regions where the transition occurs. We also seek to understand the relationship between the character of the transition along individual trajectories, and the climatological transition evident in seasonally

ACPD
9, 23589–23622, 2009

averaged maps of cloudiness.

To answer these questions we make use of the emergence of new capabilities from satellite remote sensors and of improved reanalysis of meteorological observations. We compute a large number of Lagrangian trajectories of air parcels in the eastern subtropical oceans. The evolution of the cloud and of its environment along each of these individual trajectories is then evaluated using various observational data sets and meteorological reanalysis. We build thus a Lagrangian view of the transitions in marine boundary layer cloudiness.

Section 2 provides a description of our methodology and of the data sets employed for analyzing the downstream evolution of the air parcels. Section 3 examines whether the transition in cloudiness and its associated meteorological context differ from one ocean basin to another. The factors modulating these transitions are discussed in Sect. 4. Section 5 investigates the differences between our Lagrangian view of the transition in marine boundary layer cloudiness and the classical Eulerian view of this transition supplied by cloud climatologies, and Sect. 6 summarizes our major findings.

2 Lagrangian analysis of the air masses flow in the eastern subtropical oceans

To examine the transitions in marine boundary layer cloudiness, we first compute the trajectories of individual air parcels, using the wind fields provided by reanalysis of past observations. Then, we extract the cloud and the meteorological properties of the air parcel at different locations along these trajectories from various data sets. This Lagrangian technique of analyzing the air masses flow was previously used by Pincus et al. (1997) to examine the transition from stratocumulus to cumulus observed over the northeast Pacific in several tens of cases, and by Mauger and Norris (2007, 2009) to investigate the impact of meteorological history on the subtropical cloudiness in the northeast Atlantic.

Here we apply this technique to systematically document the transitions in marine boundary layer cloudiness in the four eastern subtropical oceans where such transi-

ACPD
9, 23589–23622, 2009

tions are likely to occur, i.e. northeast, and respectively southeast, Atlantic and Pacific (NEA, SEA, NEP, SEP hereafter). Our analysis covers a six months period centered around the month of maximum cloud fraction in each basin (i.e. May to October for the Northern Hemisphere and July to December for the southern one), and spans the period 2002–2007.

2.1 Computing trajectories

For the selected period, we compute daily trajectories in each of the four oceanic basins. The three-dimensional time evolution of air parcels is computed with the Hybrid Single-Particle Lagrangian Integrated Trajectory Model (HYSPLIT) (http://www.arl.noaa.gov/HYSPLIT_info.php) using gridded meteorological fields from the interim reanalysis of the European Centre for Medium-Range Weather Forecasts – the ERA-INTERIM. We initialize the trajectories within the boundary layer at a height of 200 m above sea level. This level was chosen to be well within the boundary layer, yet avoid undue influence from the surface.

We initialize trajectories at nine equally spaced points within each of four $10^{\circ} \times 10^{\circ}$ boxes where stratocumulus decks occur most frequently (black squares in Fig. 1, after Table 1 of Klein and Hartmann, 1993), which yields approximately 10 000 trajectories for each region (Table 1). Each trajectory begins at 11 local time (LT) and lasts for six days. To identify the provenance of the analyzed air masses, we also perform two sets of daily backward trajectories using the same starting points, starting time and duration as for the forward trajectories. For the second set of backward trajectories, we consider an initial height of 2000 m above sea level.

2.2 Characterizing the clouds and their environment

To document the evolution of the air masses properties along each of the forward trajectories, we use observations from the Moderate Resolution Imaging Spectroradiometer (MODIS); the Advanced Microwave Scanning Radiometer for Earth Observing System

ACPD
9, 23589–23622, 2009

(AMSR-E) and from the Global Precipitation Climatology Project (GPCP). Additionally we evaluate the meteorological state along the trajectories using data provided by the ERA-INTERIM.

As HYSPLIT provides hourly locations of the air parcels along the trajectories, every time an observation/reanalysis field is available, we can extract the cloud or the environmental properties supplied by this field at the corresponding location of the air parcel. Each of the air parcels properties is computed as the average of all data from grid boxes within 1° of the air parcel location at the observation/reanalysis time. Because the various data sets have slightly different spatial resolution, this will represent the average over a somewhat slightly bigger or smaller area depending on the data set's resolution. The following paragraphs indicate which data sets are used to characterize the Lagrangian evolution of the clouds and of their environment.

2.2.1 Environmental properties

For the environmental properties, we use the gridded meteorological fields of ERA-INTERIM reanalysis, which have a spatial resolution of 1.5° × 1.5° and a temporal resolution of 6 h. From this data set, we use the wind fields at 10 m, the temperature at 2 m and the vertical profiles of wind, temperature and relative humidity to compute the trajectories of air parcels with HYSPLIT. Additionally, along each trajectory we extract the SST, the large scale divergence and the profiles of specific humidity and temperature.

2.2.2 Cloud and aerosol properties

We describe the cloud fraction, the cloud optical thickness and the aerosol optical depth along the trajectories from the Collection 5 of the MODIS Level-3 products (Platnick et al., 2003; King et al., 2003), which contain global gridded statistics at a resolution of 1° × 1°. We use data from both the Terra and Aqua platforms, so that two measurements per day are available, shortly after their equatorial crossing times of 10:30 and 13:30 respectively. Cloud and aerosol products are available only during daylight. We use

the Cloud_Fraction_Liquid product, which is derived based on the cloud optical properties retrieval algorithm. This differs from other cloud estimates available from MODIS, sometimes quite starkly, but is consistent with MODIS estimates of optical thickness and liquid water path. Details about the Cloud_Fraction_Liquid product, its use in our analysis, and the uncertainties in measuring cloud fraction are given in Appendix A.

2.2.3 Atmospheric vapor content and precipitation

We document the equatorwards evolution of the total vapor content of the atmosphere from the AMSR-E data set. AMSR-E is flying onboard Aqua, so that two measurements per day are available, at about 01:30 and 13:30, where here again the times refer to the equatorial crossing times, but these differ from local times only by a few minutes to tens of minutes depending on latitude. This data set is provided on a $0.25^{\circ} \times 0.25^{\circ}$ grid.

We also describe the evolution of the surface precipitation rate from the data set provided by the GPCP, which contains daily averages of the precipitation rate at the surface on a $1^{\circ} \times 1^{\circ}$ global grid.

2.3 Conditional sampling

We examine the characteristics of the transition in cloudiness and of its associated environmental context in each of the four subtropical oceans, based on the trajectories that are the most likely to experience such a transition. To determine these trajectories for each basin, we select those corresponding to the air parcels advected over warmer waters (southwestward in Northern Hemisphere, northwestward in the Southern Hemisphere). From those trajectories, we then choose the set of 3000 trajectories that have the highest initial cloud fraction (which roughly corresponds to 30% of the total number of trajectories). We then explore the characteristics of the distribution of cloud amount and of environmental properties over these 3000 trajectories.

3 Mean structure of the transition in cloudiness

In this section we examine the collection of Lagrangian trajectories to investigate whether the transition in cloud fraction and its controlling factors are different from one subtropical ocean basin to another.

3.1 The transition in cloud fraction

3.1.1 Spatial structure

Although we base our analysis on only about a third of all possible scenes, the cloud statistics composited over the days we sample is quite similar to the picture one gets for simple seasonal averages. This is reflected by Fig. 1, where we show the composite structure at the midpoints (day 3) of the selected trajectories. In all four regions the subtropical cloud cover is maximum within (or nearby) the stratocumulus regions of Klein and Hartmann (1993) and it decreases gradually equatorwards. The cloud fraction is higher in the southern basins, on average, than in the northern ones, with cloud fractions being markedly lower in the NEA (Klein and Hartmann, 1993). This means that trajectories in the Southern Hemisphere start at higher cloud fractions than do those north of the Equator (Table 1 and Fig. 1).

The same is true for the broad air masses circulation within the boundary layer, as the trajectories more or less follow isobars of the mean circulation, with cross-isobaric flow consistent with Ekman effects. As showed by the median backward and forward boundary layer trajectories in Fig. 1 (full lines), the trajectories predominantly follow anticyclonic paths, starting in the storm track regions in midlatitudes, passing through a maximum of cloudiness (i.e. the stratocumulus regions) and ending up in the trade winds regions.

Even if the equatorward flow of the analyzed air masses looks overall quite similar in the four regions, there are some differences, most notably between the trajectories in the two hemispheres. The air flow has a cross-equatorial component in the South-

ACPD
9, 23589–23622, 2009

ern Hemisphere. The southern trajectories seem thus to pass through a minimum of cloudiness when they cross the Equator, and they become more meridional afterwards. In the SEA roughly half the trajectories end up on the African coast, which means that they do not enter in the composites (Table 1). Consequently, the forward trajectories selected for this region start predominantly from the western half of the starting box, while in the other basins they are equally likely to start from any of the nine starting points.

The origin of the air mass above the boundary layer (dashed line in Fig. 1) differs among the four basins, originating variously from the continent (NEA), off-shore regions (SEA, NEP), and the open ocean (SEP). This indicates, among other things, that the circulations in the free troposphere and boundary layer are decoupled. (The shortness of the backward free-tropospheric trajectories reflects an unsteady flow which generates more variability among the backward trajectories, rather than lower wind speeds above the boundary layer.)

Figure 1 allowed us to highlight the similarities and differences between the sets of trajectories analyzed in the four subtropical oceans and gave an image of the average cloud fraction typical for the situations analyzed within each of these regions. To gain more quantitative information about these transitions in marine boundary layer cloudiness, we now look at the composite temporal evolution of the cloud fraction along the trajectories.

3.1.2 Temporal evolution

We examine the time evolution of the cloud fraction distribution for the 3000 trajectories analyzed in each of the four basins (Fig. 2a). Because the trajectories in the NEA start with cloud fractions lower than those in the other basins (Table 1 and Fig. 1) we adjust the initial time in this (and other) regions so that the median trajectory starts with the same value as the one from the zone with the highest cloud fraction (SEA) (for Figs. 2 and 3). This facilitates the comparison between the different regions.

From this Lagrangian perspective, the transition in cloud fraction looks similar in all

ACPD
9, 23589–23622, 2009

four subtropical oceans. As we show in Appendix A this result does not depend on our choice of cloud fraction product. In each case, the stratocumulus deck breaks-up during the first three days of the trajectories (as suggested by decrease of the median cloud fraction on day 3 to less than half of its initial value, Fig. 2a, lower panel). After this time, the air parcels enter a shallow cumulus regime and the cloud fraction suffers more subtle variations. Our identification of the first three days as the period of the transition is consistent with increased variability in cloud fraction during this period (Fig. 2a, upper panel). Such variability is precisely what we would expect if the cloud fraction is changing significantly during this period, as slight variations in the start of the transition would translate into increased variability.

The transition from stratocumulus to broken shallow cumulus fields typically occurs before the precipitation at surface becomes significant (Fig. 2b); median values of liquid water path (not shown, but see Appendix B for a discussion) also remain roughly constant along the trajectories. Both quantities, however, are difficult to measure.

3.2 The environmental context

Figure 2 shows that the transition in cloud fraction is independent of location; in this section we ask whether the relationships between cloud fraction and the environment (and hence the mechanisms of the transition) are also consistent. We do so by examining the evolution of different environmental factors that might influence the transition in cloud fraction. These include SST, the lower tropospheric stability (LTS, defined as the difference in potential temperature between 700 hPa and the surface), large-scale divergence, atmospheric vapor content, free-tropospheric humidity and the atmospheric aerosol.

All these factors evolve similarly in the four subtropical oceans, albeit with different characteristic values in each region (Fig. 3). In all four basins the transition in cloud fraction is associated with strong changes in SST, hence with strong changes in LTS (Figs. 2a, 3a and 3b). The transition is not, however, associated with significant changes in the large-scale divergence (at least on average, Fig. 3c, lower panel), or in

ACPD
9, 23589–23622, 2009

the temperature above the boundary layer (not shown). Indeed, the median large-scale divergence decreases only after the third day, when the air parcels reach convective regions. The variability in the large-scale divergence among the trajectories also increases noticeably only after the cloud break-up (Fig. 3c, upper panel). As for the temperature above the boundary layer, it changes little during the six days and if anything, decreasing slightly equatorwards. Atmospheric vapor content both within and above the boundary layer (Fig. 3d and 3e) tracks SST, and hence the transition in cloudiness, fairly well, since precipitable water is closely linked to surface temperature. It is possible that the gradual humidification of the free-troposphere (Fig. 3e) might affect cloud evolution through its impacts on the cloud-top radiative cooling and drying of the cloud layer via mixing at its top, but these impacts are likely of secondary importance.

Aerosol optical depth (AOD) varies significantly among the basins, with values along the Atlantic trajectories twice as large as along the Pacific ones (Fig. 3f, lower panel), consistent with the origins of free tropospheric air along the trajectories (i.e. the African continent for NEA and SEA, predominantly oceanic regions for NEP and SEP, Fig. 1). The transition in cloud cover is nonetheless quite similar in the Atlantic and Pacific oceans (Fig. 2a). This might be interpreted as an insensitivity of the transition to aerosol indirect effects, though it is also possible that aerosol coming from the African coast remains above the boundary layer and does not interact with the cloud layer.

Our results seem to corroborate the hypothesis that the SST increase, and the associated LTS decrease, are the main driving factors of the transition in cloud fraction (Bretherton, 1992).

4 What differentiates fast and slow transitions?

To gain a deeper insight about the causes of the transition, we investigate in this section what differentiates the fast and the slow transitions taking place in each region. For that purpose, we compare the distributions of cloud properties and of meteorological forcings obtained for two distinct subsets of the 3000 trajectories analyzed in each

region: the trajectories experiencing the fastest, and respectively the slowest transitions in cloud fraction. To select these subsets, we first average the cloud fraction over the first three days of the trajectories. Then, we pick the 25% of the 3000 trajectories having the lowest, and respectively the highest, values for this 3-days average cloud fraction. Hereinafter, we illustrate this comparison only for the NEP (Figs. 4 and 5). However, consistent results are found for the other oceanic basins.

Trajectories experiencing slow transitions usually come from upstream (eastern part of the starting box) relative the ones experiencing fast transitions. It appears that the differences between the two subsets of trajectories discussed herein (Fig. 4) are mainly due to the geographical location of the starting points. The trajectories starting closer to coasts have to cross the entire stratocumulus region, so it is expected that the cloud breaks-up latter than for the trajectories starting more downstream. And indeed, if the temporal rescaling applied for comparing the transition in the four basins is applied here (by rescaling the time axis so that the trajectories experiencing fast and slow transitions start at the same median LTS), the spread in cloud fraction between the two subsets is reduced by a factor of two. We suspect that the remaining spread simply reflects the fact that the meteorological regime will shift with time for a given starting point in space; that is trajectories starting from a given point may transition more slowly to cumulus clouds during periods with anomalously cold surface waters.

The environments in which the transitions occur are mainly distinguished by their values of SST and LTS (Fig. 5a and b). The rate of change in SST or LTS along the trajectory, is however more or less constant between the two categories of the transition (Fig. 5a and b). Likewise, there appears to be little difference between the initial characteristics of the clouds, including median cloud fractions (Fig. 4a) and optical thickness (not shown). Other aspects of the meteorological environment are also more or less the same for the two categories of trajectories (large-scale divergence, total vapor path, free-tropospheric humidity, AOD; Fig. 5c, d, e and f).

This suggest that the time scale of the transition depends on the values of the SST and LTS rather than on their along-trajectory gradient, consistent with previous work

ACPD
9, 23589–23622, 2009

linking LTS and the low-level cloud cover (Klein and Hartmann, 1993; Pincus et al., 1997; Mauger and Norris, 2009). The line of arguments behind this idea is that a stronger inversion (hence a stronger LTS) limits the efficiency of mixing of drier and warmer free-troposphere air at cloud top. This helps maintain a humid boundary layer driven predominantly by cloud top cooling, which is in turn conducive to a well-mixed layer.

5 Composite versus climatological transition

The Lagrangian analysis of the individual trajectories emphasized physical properties associated with the transformation of air masses as they flow equatorwards, away from the stratocumulus regions that prevail over eastern boundary-current regions (Table 1). However, no striking differences appear between the Eulerian view of the transition in cloud fraction obtained by averaging over the days when such a transition is evident (e.g., Fig. 1 which shows the composite over days when transitions are identified and are at their mid point) and the one supplied by simple averages over the months with maximum subtropical cloudiness (Fig. 6). This leads to the idea that the transitions between stratocumulus and cumulus are a persistent feature of the subtropical oceans during these months. To explore this idea more thoroughly, in this section we investigate whether the transitions are sufficiently prevalent (or characteristic) that the climatological fields reproduce their characteristics. For that, we examine the extent to which the characteristics of these transitions, emphasized by the Lagrangian analysis of individual trajectories, are similar to the ones reflected by simple climatological averages.

The underlying interest for this question is related to the disadvantages of the Lagrangian approach compared to an Eulerian one (which would use climatological fields to describe the transition). The Lagrangian analysis of a large number of trajectories requires a huge amount of data and time. Moreover, the respective data sets that one wishes to analyze along a trajectory must have a sufficiently good spatial and tempo-

ACPD
9, 23589–23622, 2009

ral coverage to ensure coverage over what ends up being a sparse set of trajectories. Which adds another inconvenience. Namely, it limits the satellite remote sensors that can be used for the Lagrangian analysis to those with a wide scan swath (like MODIS). And it excludes thus the possibility to use finer scale instruments that supply high quality products but have a narrow swath (like for e.g. the Multiangle Imaging SpectroRadiometer MISR, the Cloud-Aerosol Lidar Infrared Pathfinder Satellite Observation CALIPSO or CloudSat).

To address these issues, we compare the composite transition build from our Lagrangian analysis with a climatological transition. By climatological transition, we mean the transition which takes place following streamlines of the climatological (or average) flow. Furthermore, the nature of the climatological transition is explored in terms of the properties taken from the climatological fields of various cloud and meteorological data sets. This, mean field, approach is currently used by the GEWEX Pacific Cross-Section Intercomparison (GPCI) working group of GEWEX Cloud System Study (GCSS) to explore the transition between different cloud regimes over the NEP (Teixeira et al., 2009).

We focus only on the three months with the highest cloud fraction in the stratocumulus region of each oceanic basin. That is June/July/August (JJA hereafter) for the northern basins, and September/October/November (SON hereafter) for the southern ones (Klein and Hartmann, 1993). As it turns out our transition trajectories in the Northern Hemisphere predominantly come from this three month period of maximum cloud fraction, while in the Southern Hemisphere transition trajectories were more evenly distributed across the original six month period. For consistency we select the three month period of maximum cloud fraction for both hemispheres.

We first construct a composite transition from the individual forward trajectories (Sect. 2.1). For that, we follow the methodology used in Sect. 2.3 for the six month period, but we restrict ourselves to the three month period described above. The median trajectory and the medians of the distributions of the air masses properties over the analyzed set of trajectories will be referred to hereafter as the characteristics of the composite transition.

ACPD
9, 23589–23622, 2009

Secondly, we construct a climatological transition for each region. This is defined as the trajectory following the climatological streamlines and is constructed by initializing HYSPLIT with the gridded meteorological ERA-INTERIM fields corresponding to the mean JJA/SON day (over all JJA/SON from 2002 to 2007). In each region, we consider the same nine starting points, starting time and duration as for the individual forward trajectories (Sect. 2.1). We then characterize the transitions along these nine trajectories by extracting the different cloud and meteorological properties from the averages over all JJA/SON from 2002 to 2007 of the respective data fields. As for the set of individual daily trajectories, we then compute for this set of climatological trajectories the median trajectory and the medians of the distributions of the cloud and meteorological variables (that we will further refer to as the characteristics of the climatological transition). The coordinates of these median climatological trajectories are made available in Appendix C.

The climatological trajectory is very close to the composite one for the northern oceans (Fig. 6). More noticeable differences occur in the southern oceans, and more particularly in the SEA. In these regions the flow is less steady and more meridional, so a lower percentage of the trajectories fulfill the primary condition required to be included in the composites, i.e. to go over warmer waters (only 54% in SEA and 70% in SEP against 82% and 88% in NEA and NEP, respectively).

The climatological transition in cloud fraction has the same character as the composite one in all regions (Fig. 7). To the extent that the initial cloud fraction is somewhat lower, the transition is less abrupt. This is not unexpected since the composite transition includes only the trajectories with a high initial cloud fraction, while the climatological JJA/SON fields used to describe the cloud fraction along the climatological trajectories include all situations. In the SEA, some differences also occur during the last 2 days, when the discrepancies between the climatological and composite trajectories are the most pronounced. Indeed, the climatological trajectory gets more meridional in the vicinity of the Equator, so the air parcel following it ends up closer to the coasts, in regions with higher cloud fraction (Fig. 6). The time evolution of the meteorological

ACPD
9, 23589–23622, 2009

properties along the two trajectories is also very similar in all four regions (not shown).

The transition in marine boundary layer cloudiness appears robustly in the climatological fields. Robustly enough for the mean fields to well represent the evolution of actual trajectories (at least for the seasons analyzed). In some sense this may simply reflect the steadiness of the trade winds in these regions. This result has important implications for both observational and modeling studies of the transitions in marine boundary layer cloudiness. As it implies that satellite observations with a more limited footprint and temporal coverage and which thus insufficiently sample individual trajectories, could, by documenting the structure of the climatological transition, provide meaningful constrains on the evolution of the cloud field. Thus, average fields of CALIPSO, CloudSat or MISR products could be for example used to investigate the cloud fraction, the cloud vertical structure, the precipitation and the cloud top evolution along the climatological streamlines. In addition, our analysis suggests that averaged forcings can be considered as representative of individual trajectories. And can therefore be used to initialize numerical simulations of the transition between the two cloud regimes.

6 Conclusions

Satellite data sets and reanalysis of meteorological observations were used to document the transition between marine stratocumulus and shallow cumulus encountered in four subtropical oceans (NEA, NEP, SEA and SEP). The Lagrangian analysis of a large number of air parcel trajectories allowed us to answer, at least to some extent, the questions raised in the introduction. Based on this analysis we find that:

– the basic character of the transition in cloud fraction does not depend on the oceanic basin. In all four regions, the cloud fraction decreases sharply during the first three days, while it evolves more gradually during the last three days as the air masses move deeper into the trades.

– the environment in which the transition occurs is also similar across the four subtropical ocean basins we consider. In all four basins the transition in cloud fraction is associated with strong SSTs increases, an almost commensurate decrease in LTS and gradual humidification of the free troposphere, while the large-scale divergence and the temperature above the boundary layer are roughly constant during the transition period. Significant precipitation at the surface and marked changes in the large-scale divergence are only observed after the transition in cloudiness. The transition time scale seems to be mostly related to the strength of the LTS (which is governed by the SST) during the first part of the trajectories or prior to their starting time (Klein and Hartmann, 1993; Pincus et al., 1997; Mauger and Norris, 2009).

– the transitions in marine boundary layer cloudiness are a robust feature of the eastern subtropical oceans, during the months with maximum cloudiness in these regions. Their characteristics, depicted by the analysis of individual air parcel trajectories, are thus quite accurately reproduced by climatological (or averaged) data sets. This result justifies the use of high-resolution sensors (whose spatial coverage requires extensive temporal averaging) to study the climatological transition. As our analysis emphasizes that in most important respects the climatological transition is representative of individual transitions in cloudiness in all of the ocean basins.

Our analysis identifies important environmental factors, or changes, associated with the transition from stratocumulus to cumulus. However, it does not allow us to quantify the relative importance of these factors. And although it seems likely, based on this analysis, that the transition is driven by sharp changes in lower-tropospheric stability as air advects over warmer water, other factors, such as the effects of the humidification of the free troposphere, or the effects of very weak drizzle on boundary layer stratification and dynamics, can not be ruled out. The data analysis performed in this study will therefore be used in the future for initializing/constraining fine scale numerical

ACPD
9, 23589–23622, 2009

simulations designed to quantify the relative role of these factors, thereby more clearly establishing the chain of causality in the evolution of the low-level cloud fields of the subtropical oceans.

Appendix A

Measuring cloud fraction

The most dramatic aspect of the transition from stratocumulus to shallow cumulus is the rapid reduction in cloud fraction. This quantity is normally determined by using one or more continuous fields (radiances at one or more wavelengths) as inputs to a decision tree; the result is a binary mask in which each pixel is classified as "cloudy" or "clear". Some proportion of pixels are likely too near to whatever thresholds are used to segregate clouds into these categories, so the precise value of cloud fraction can depend strongly on particular algorithmic choices. In this appendix we demonstrate that the precise value of cloud fraction during the transition is ambiguous, but that the behavior of the transition is independent of the algorithms used to determine cloud fraction.

The algorithms used by MODIS to retrieve cloud properties operate in several steps. The first, called the "cloud mask" (Frey et al., 2008; Ackerman et al., 2008) attempts to distinguish those pixels that are likely to contain cloud from those that are entirely clear. This decision is expressed as four confidence levels, and those pixels classified as "cloudy" or "probably cloudy" are further analyzed to determine the cloud thermodynamic phase (ice or liquid) and optical properties (optical thickness and particle size). But in some number of cases it is not possible to identify a combination of phase, particle size, and optical thickness consistent with the observed reflectances at multiple wavelengths. This may occur because the pixel has been mis-classified as cloudy, as is common in regions of sun-glint (Zhao and Girolamo, 2006). In the Collection 5 retrievals used here, pixels adjacent to clear sky are also rejected, as these are subject

ACPD
9, 23589–23622, 2009

to retrieval biases.

We determine the boundary-layer cloud fraction using the MODIS "Cloud_Fraction_Liquid" product which represents the proportion of pixels in each 1° cell for which retrievals of optical thickness and particle size were successfully performed (and for which the blackbody emission temperature exceeds 273 K). We eliminate the possibility of masking by high clouds by excluding cells whose value of "Cloud_Fraction_Ice" exceeds 5%. As an alternative, we might have used the proportion of pixels determined "cloudy" or "probably cloudy" by the cloud mask. This value is available as "Cloud_Fraction_Day" and it is substantially higher than the "Cloud_Fraction_Liquid" following the trajectories we selected (Fig. A1, panel a). To the extent that cloud fraction could be determined less ambiguously (by using instruments with much higher spatial resolution, for example), the two cloud fraction products are likely to bound this value.

But the behavior of the transition does not depend on the precise value of cloud fraction. Figure A1, panel b, shows the transition determined using the median value of both products along the trajectory, where the cloud fraction has been scaled as (CF(t)-CF(t=6 days))/(CF(t=0)-CF(t=6 days)). We show results for the NEP here, but the behavior is identical in all regions, namely that cloud fraction decreases from its maximum value (near 1 in both products) to its minimum (approx. 20% for "Cloud_Fraction_Liquid" and 60% for "Cloud_Fraction_Day") over the space of three days, with the bulk of the transition occurring in days three and four.

We infer that the transition is not an artifact of how one measures cloud fraction.

Appendix B

Measuring the liquid water path

LWP retrievals are generally subject to different sources of error (Chellappan and Horvath, 2009), which lead to considerable discrepancies between the LWPs provided by

ACPD
9, 23589–23622, 2009

different sensors. Chellappan and Horvath (2009) emphasize for example the systematic differences between the Wentz algorithm used by AMSR-E and the optical LWP retrieval performed by MODIS. Namely, MODIS overestimates AMSR-E LWP in overcast domains, but it noticeably underestimates it in broken scenes (Table 1 in Chellappan and Horvath (2009)). Even if to some extent microwave retrievals can be considered more trustful than the optical retrievals of the LWP, the Wentz (microwave) algorithm has its own sources of error, such as for e.g. the cloud-rain partitioning (Chellappan and Horvath, 2009). This cloud-rain partitioning is performed whenever the cloud total water path retrieved with Wentz algorithm is superior to 180 gm^{-2}. The applied rain parameterization is however rather simplistic, being based on a study of NEP extratropical cyclones.

We used both AMSR-E and MODIS datasets to examine the evolution of the LWP along the trajectories. Our analysis corroborates the noticeable differences between the two instruments found by Chellappan and Horvath (2009) (not shown). We show here as an example the temporal evolution of the LWP distribution obtained from AMSR-E data set (Fig. B1). The transition between the two clouds regimes is less evident in LWP than in cloud fraction, even if the diurnal cycle is more marked (Fig. B1, lower panel). The variability among trajectories increases when the air parcels penetrate a convective regime (after the third day, Fig. B1, upper panel). Note however that the caveats of Wentz algorithm should be kept in mind while analyzing these results.

Appendix C

Climatological trajectories

For readers interested in further analyzing these transitions in marine boundary layer cloudiness, we include here (Table C1) the coordinates of the climatological trajectories performed in the four oceanic basins.

Acknowledgements. ECMWF ERA-INTERIM data used in this study have been obtained from

the ECMWF data server (http://www.ecmwf.int/products/data/). AMSR-E data are provided by the Remote Sensing Systems (http://www.remss.com/amsr/amsr_browse.html), and GPCP data have been obtained from the website http://precip.gsfc.nasa.gov/. Roland Draxler is thanked for his help with the HYSPLIT model provided by ARL-NOAA (http://www.ready.noaa.gov/ready/hysplit4.html). We also acknowledge Larry di Girolamo, Steve Ackerman and Steven Platnick for the clarifying discussions concerning the Level-3 MODIS cloud products. This work was supported by Alexander von Humboldt foundation and the Max Planck for Meterorology. The service charges for this open access publication have been covered by the Max Planck Society.

References

Ackerman, S. A., Holz, R. E., Frey, R., Eloranta, E. W., Maddux, B. C., and McGill, M.: Cloud Detection with MODIS. Part II: Validation, J. Atmos. Ocean. Tech., 25, 1073–1086, 2008. 23606

Albrecht, B. A., C.S.Bretherton, D.W.Johnson, W.H.Schubert, and Frisch, A. S.: Atlantic Stratocumulus Transition Experiment – ASTEX, B. Am. Meteor. Soc., 76, 889–904, 1995. 23591

Bretherton, C. S.: A conceptual model of the stratocumulus-trade-cumulus transition in the subtropical oceans, ICCP proceedings, 374–377, 1992. 23591, 23599

Bretherton, C. S. and Pincus, R.: Cloudiness and Marine Boundary Layer Dynamics in the ASTEX Lagrangian Experiments. Part I: Synoptic setting and vertical structure, J. Atmos. Sci., 52, 2797–2723, 1995. 23591

Bretherton, C. S. and Wyant, M. C.: Moisture. transport, lower-troposphere stability, and. decoupling of cloud-topped boundary, J. Atmos. Sci., 54, 148–167, 1997. 23591

Bretherton, C. S., Krueger, S. K., Wyant, M. C., Bechtold, P., van Meijgaard, E., Stevens, B., and Teixeira, J.: A GCSS boundary layer model intercomparison study of the first ASTEX Lagrangian experiment, Bound.-Lay. Meteorol., 93, 341–380, 1999. 23591

Chellappan, S. and Horvath, A.: Global assessment of AMSR-E and MODIS Cloud Liquid Water Path Retrievals in Warm Oceanic Clouds, J. Geophys. Res., under review, 2009. 23607, 23608

De Roode, S. and Duynkerke, P.: Observed Lagrangian transition of stratocumulus into cumulus

during ASTEX: Mean state and Turbulence structure, J. Atmos. Sci., 54, 2157–2173, 1997. 23591

Frey, R., Ackerman, S. A., Liu, Y., Strabala, K. I., Zhang, H., Key, J. R., and Wang, X.: Cloud Detection with MODIS. Part I: Improvements in the MODIS Cloud Mask for Collection 5, J. Atmos. Ocean. Tech., 25, 1057–1072, 2008. 23606

King, M., Menzel, W., Kaufman, Y., Tanre, D., Bo-Cai Gao; Platnick, S., Ackerman, S., Remer, L., Pincus, R., and Hubanks, P.: Cloud and aerosol properties, precipitable water, and profiles of temperature and water vapor from MODIS, Geosci. Remote Sens., 41, 442–458, 2003. 23594

Klein, S. A. and Hartmann, D. L.: The Seasonal Cycle of Low Stratiform Clouds, J. Climate, 6, 1587–1606, 1993. 23590, 23593, 23596, 23601, 23602, 23605, 23614

Klein, S. A. and Norris, J. R.: On the Relationships among Low-Cloud Structure, Sea Surface Temperature, and Atmospheric Circulation in the Summertime Northeast Pacific, J. Climate, 8, 1140–1155, 1995. 23591

Krueger, S. K., McLean, G. T., and Fu, Q.: Numerical Simulation of the Stratus-to-Cumulus Transition in the Subtropical Marine Boundary Layer. Part I: Boundary-Layer Structure, J. Atmos. Sci., 52, 2839–2850, 1995. 23591

Malkus, J. and Riehl, H.: Cloud structure and distributions over the tropical pacific ocean, University of California Press, Berkley and Los Angeles, California, USA, 1964. 23590

Mauger, G. S. and Norris, J.: Meteorological bias in satellite estimates of aerosol-cloud relationships, Geophys. Res. Lett., 34(16), L16824, doi:10.1029/2007GL029952, 2007. 23592

Mauger, G. S. and Norris, J.: Assessing the Impact of Meteorological History on Subtropical Cloud Fraction, J. Climate, 2009. 23592, 23601, 23605

McDonald, W.: Atlas of climatic charts of the oceans, U.S. Dept. of Agriculture, Weather Bureau, Washington, DC, USA, 1938. 23590

Neiburger, M., Johnson, D., and Chien, C.: Studies of the structure of the atmosphere over the eastern pacific ocean in summer. I. The inversion over the Eastern North Pacific Ocean, University of California Press, Berkley and Los Angeles, California, USA, 1961. 23590

Pincus, R., Baker, M., and Bretherton, C.: What controls stratocumulus radiation properties? Lagrangian observations of cloud evolution, J. Atmos. Sci., 54, 2215–2236, 1997. 23591, 23592, 23601, 23605

Platnick, S., King, M. D., Ackerman, S. A., Menzel, W. P., Baum, B. A., Ridi, J. C., and Frey, R. A.: The MODIS Cloud Products: Algorithms and Examples From Terra, IEEE T. Geosci.

Remote Sens., 41, 459–473, 2003. 23594
Schubert, W., Wakefield, J. S., Steiner, E. J., and Cox, S. K.: Marine Stratocumulus Convection. part II: Horizontally Inhomogeneous Solutions, J. Atmos. Sci., 36, 1309–1324, 1979. 23591
Stevens, B.: Cloud-transitions and decoupling in shear-free stratocumulus topped boundary layers, Geophys. Res. Lett., 27, 2557–2560, 2000. 23591
Teixeira, J., Cardoso, S., Bonazzola, M., Cole, J., DelGenio, A., Demott, C., Ffranklin, C., Hannay, C., Jakob, C., Jiao, Y., Karlsson, J., Kitagawa, H., Koehler, M., Kuwano-Yoshida, A., LeDrian, C., Lock, A., Miller, M., Marquet, P., Martins, J., Mechoso, C. R., Meijgaard, E. V., Meinke, I., Miranda, P., Mironov, D., Neggers, R., Pan, H., Randall, D., Rasch, P., Rockel, B., Rossow, W. B., Ritter, B., Siebesma, A., P.Soares, Turk, F., Vaillancourt, P., von Engeln, A., and Zhao, M.: Tropical and sub-tropical cloud transitions in weather and climate prediction models: the GCSS/WGNE Pacific Crosssection Intercomparison (GPCI), J. Climate, submitted, 2009. 23602
Von Ficker, H.: Die Passatinversion, Veroffentl. d. Meteorol. Inst. d. Univ. Berlin, I, Heft 4, 1936. 23590
Wyant, M., Bretherton, C., Rand, H., and Stevens, D.: Numerical simulations and a conceptual model of the subtropical marine stratocumulus to trade cumulus, J. Atmos. Sci., 54, 168–192, 1997. 23591
Zhao, G. and Girolamo, L. D.: Cloud fraction errors for trade wind cumuli from EOS-Terra instruments, Geophysical Res. Lett., 33, L20802, doi:10.1029/2006GL027088, 2006. 23606

Table 1. Total number of trajectories, percentage going over warmer waters (SW in the Northern Hemisphere, NW in the Southern Hemisphere), range of the initial MODIS Terra liquid cloud fraction for the selected 3000 trajectories.

Zone	Total number of trajectories	percentage going over warmer waters (%)	range of the initial cloud fraction for the selected 3000 trajectories
NEA	9936	73.	[0.386–1]
SEA	9882	53.71	[0.886–1]
NEP	9936	85.7	[0.915–1]
SEP	9882	72.25	[0.9–1]

ACPD
9, 23589–23622, 2009

Table C1. The latitude and longitude (degrees) along the climatological trajectories of the four subtropical regions, as described in Sect. 5. The positive/negative signs correspond to the Northern/Southern Hemispheres and to east/west directions, respectively.

Hours	NEA	SEA	NEP	SEP
0	20.00, −30.00	−15.00, 5.00	25.00, −125.00	−15.00, −85.00
6	19.05, −31.34	−13.93, 3.94	24.00, −125.60	−14.11, −86.34
12	18.16, −32.78	−12.81, 2.92	23.08, −126.4	−13.09, −87.68
18	17.37, −34.24	−11.71, 1.83	22.29, −127.26	−12.12, −89.17
24	16.62, −35.68	−10.70, 0.65	21.44, −128.23	−11.26, −90.71
30	15.87, −37.16	−9.76, −0.48	20.54, −129.31	−10.43, −92.18
36	15.18, −38.70	−8.73, −1.55	19.71, −130.55	−9.45, −93.60
42	14.52, −40.28	−7.69, −2.65	18.98, −131.77	−8.54, −95.06
48	13.92, −41.73	−6.76, −3.77	18.20, −133.05	−7.70, −96.55
54	13.36, −43.15	−5.83, −4.91	17.37, −134.38	−6.84, −97.99
60	12.82, −44.57	−4.81, −5.62	16.57, −135.59	−5.91, −99.11
66	12.29, −46.01	−3.80, −5.73	15.84, −136.58	−5.08, −100.03
72	11.80, −47.41	−2.82, −5.72	15.14, −137.55	−4.29, −100.85
78	11.42, −48.73	−1.82, −5.65	14.44, −138.48	−3.43, −101.55
84	11.02, −50.04	−0.82, −5.45	13.77, −139.42	−2.57, −102.09
90	10.65, −51.40	−0.19, −5.14	13.15, −140.32	−1.82, −102.50
96	10.33, −52.73	1.23, −4.79	12.60, −141.22	−1.07, −102.76
102	10.16, −54.00	2.23, −4.61	12.14, −142.12	−0.18, −103.24
108	9.96, −55.29	3.12, −4.43	11.7, −143.07	0.73, −104.08
114	9.69, −56.58	3.88, −4.15	11.31, −144.02	1.60, −104.82
120	9.52, −57.83	4.42, −3.88	10.99, −145.38	2.54, −105.42
126	9.51, −59.01	4.58, −3.89	10.53, −146.73	3.59, −105.88
132	9.47, −60.21	4.68, −3.90	10.34, −148.04	4.57, −105.17
138	9.45, −61.34	4.69, −3.81	10.27, −149.32	5.36, −106.37
144	9.62, −62.43	4.86, −3.71	9.80, −150.58	5.95, −106.46

ACPD
9, 23589–23622, 2009

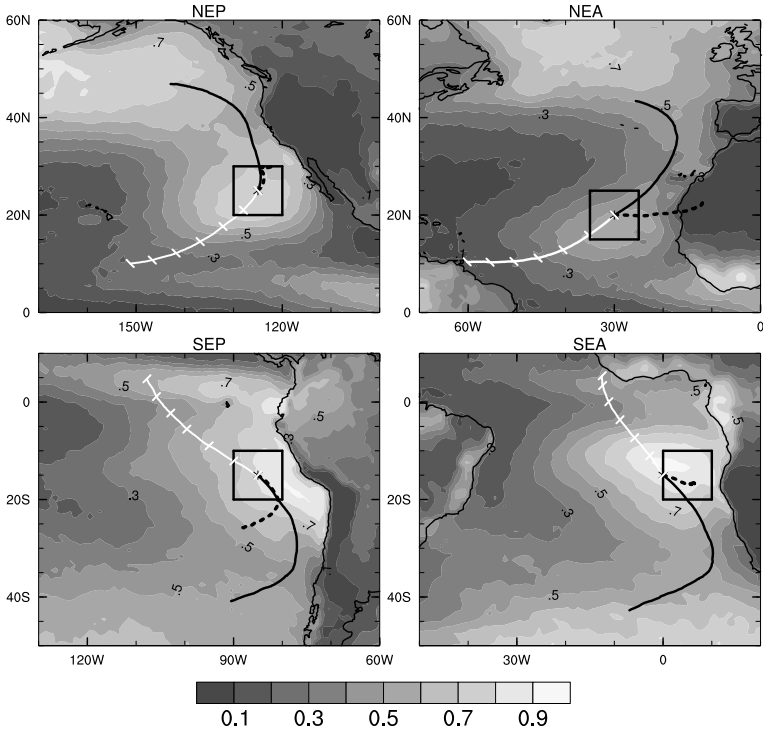

Fig. 1. Average of MODIS Terra (morning) liquid cloud fraction over the third day of the selected trajectories, and medians of the forward (white lines) and the backward (black lines) sets of trajectories analyzed in each zone. The full black lines correspond to the backward trajectories initiated at 200 m and the black dashed lines to the ones initiated at 2000 m. The tickmarks on the median of the forward trajectories indicate the position of the air parcel every 24 h. The squares indicate the stratocumulus regions studied by Klein and Hartmann (1993).

ACPD
9, 23589–23622, 2009

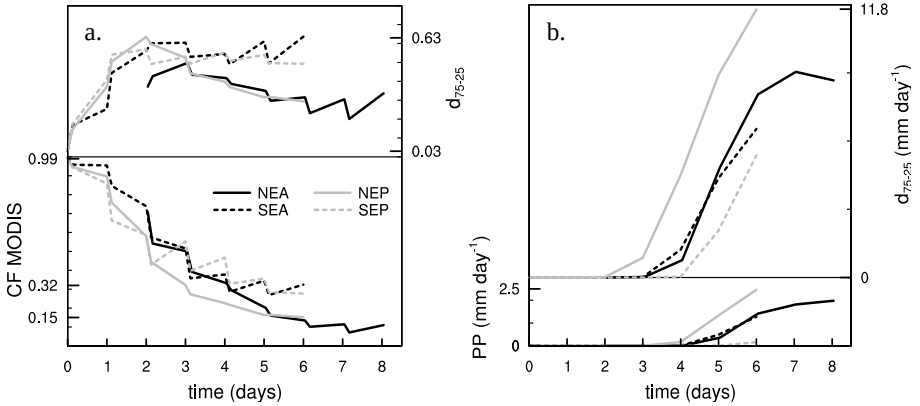

Fig. 2. MODIS liquid cloud fraction and GPCP precipitation rate along the trajectories. The lower panels show the evolution of the medians, and the upper panels illustrate the interquartile spread (i.e., the distance between the third and first quartile) of the distribution of the two variables for the sets of trajectories analyzed in each of the four subtropical oceans. In the lower panel, the y-axis labels the values at the initial time, after 3 days and respectively at the end of the trajectories; in the upper panel, it labels the minimum and the maximum values of the interquartile spread.

ACPD
9, 23589–23622, 2009

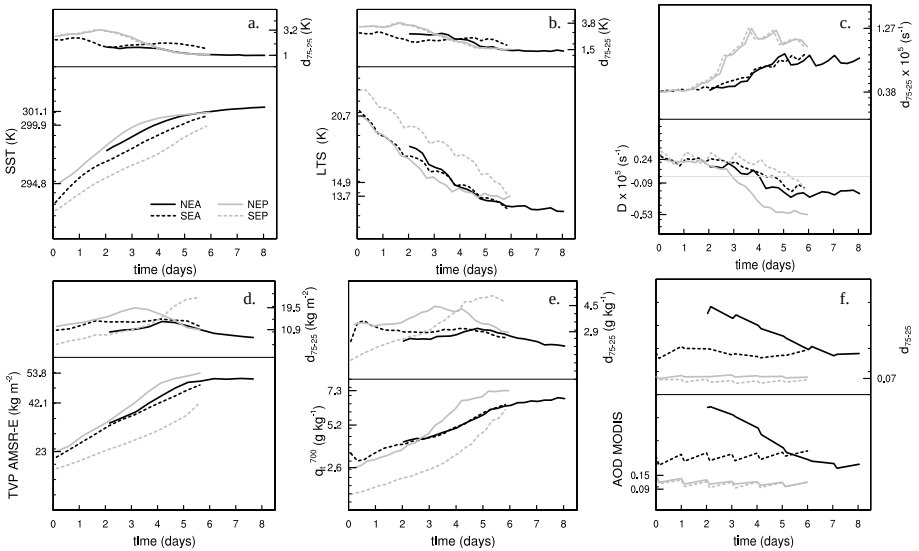

Fig. 3. Environmental factors along the trajectories: SST, lower tropospheric stability (LTS), large-scale divergence (D), AMSR-E total vapor path, specific humidity at 700 hPa and aerosol optical depth. Plotting conventions follow those in Fig. 2.

ACPD
9, 23589–23622, 2009

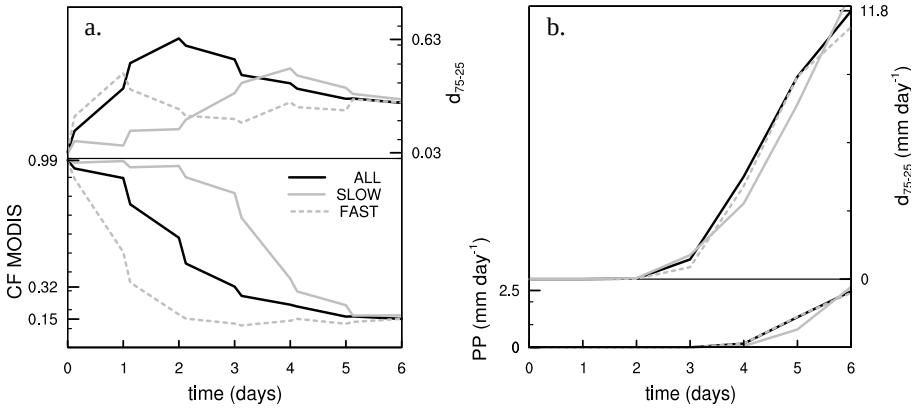

Fig. 4. Same as Fig. 2 for the set of trajectories analyzed for the NEP (black line), and for its subsets corresponding to the slowest (solid grey line) and respectively the fastest transitions (dashed grey line).

ACPD
9, 23589–23622, 2009

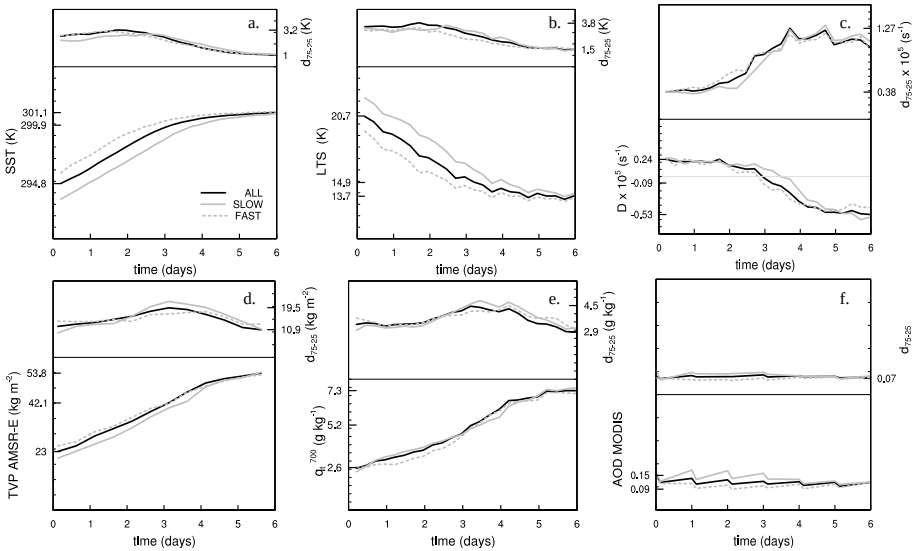

Fig. 5. Same as Fig. 3 for the set of trajectories analyzed for the NEP (black line), and for its subsets corresponding to the slowest (solid grey line) and respectively the fastest transitions (dashed grey line).

ACPD
9, 23589–23622, 2009

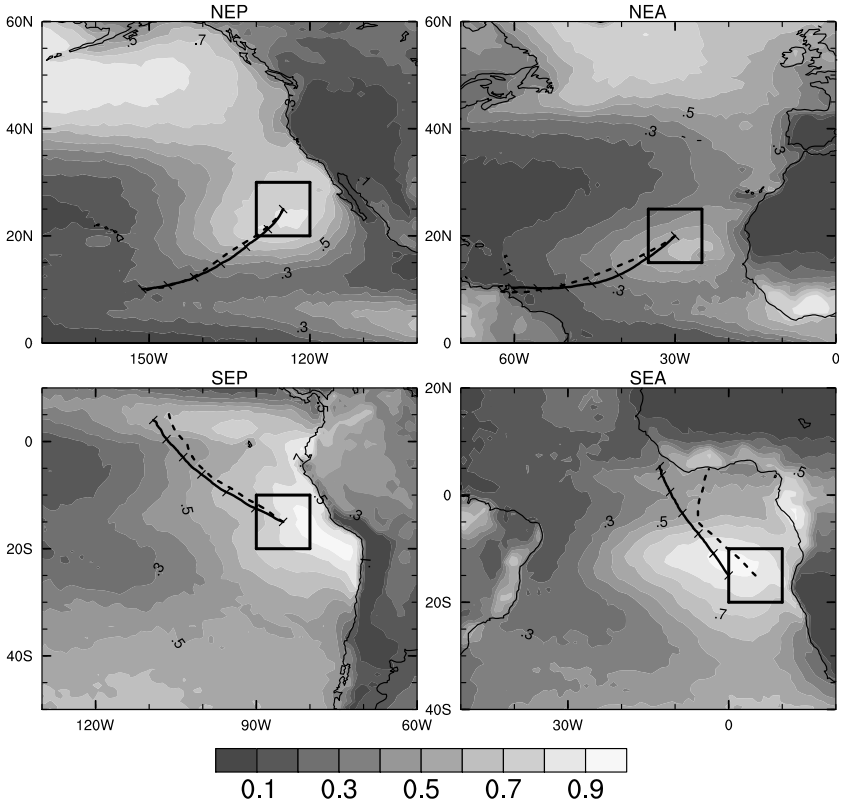

Fig. 6. Average of MODIS Terra (morning) liquid cloud fraction over JJA (NEP, NEA), and respectively SON (SEP, SEA), median of the set of individual trajectories analyzed for these months (full line), and median of the trajectories along the climatological streamlines (dashed line), for the four subtropical oceans.

ACPD
9, 23589–23622, 2009

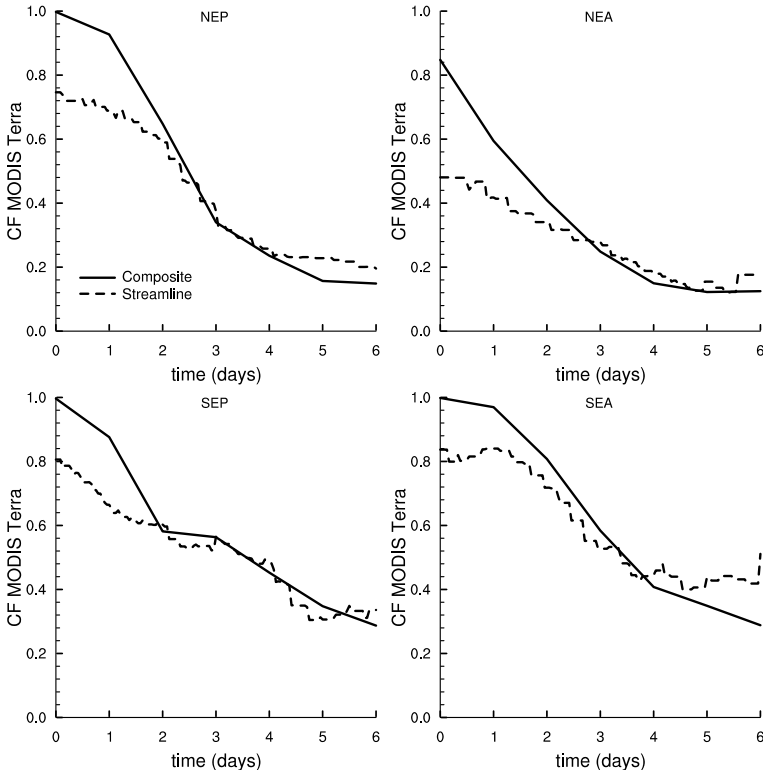

Fig. 7. Median of MODIS Terra liquid cloud fraction distribution: for the set of individual trajectories analyzed for JJA (NEP, NEA), and respectively SON (SEP, SEA) (full line) and for the set of trajectories along the climatological streamlines (dashed line), for the four subtropical oceans.

ACPD
9, 23589–23622, 2009

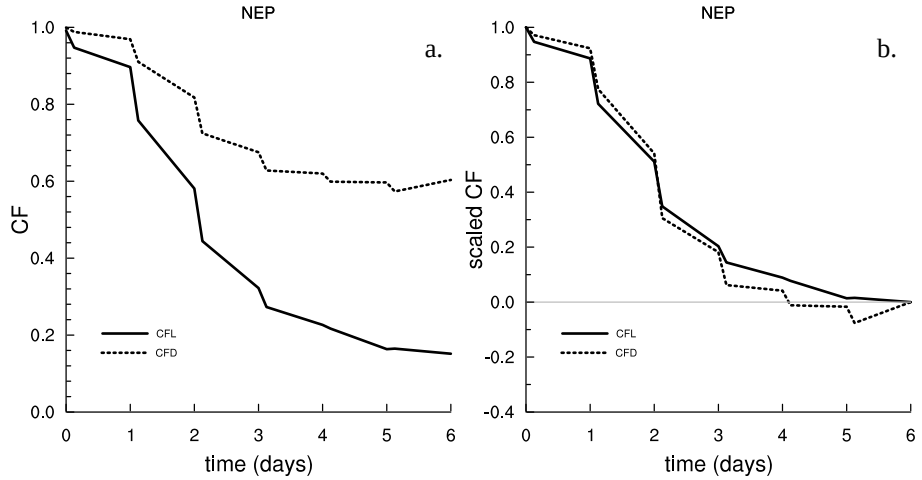

Fig. A1. (a) Time evolution of the median of MODIS "Cloud_Fraction_Liquid" (CFL, full lines) and "Cloud_Fraction_Day" (CFD, dashed lines) distributions for the set of trajectories analyzed for the NEP. For both cloud fraction products only the ice-free pixels (i.e. CFI <5%) are used to derive these distributions. **(b)** Time evolution of the medians of "Cloud_Fraction_Liquid" and "Cloud_Fraction_Day" distributions, scaled as $(CF(t) - CF(t = 6 \text{ days}))/(CF(t = 0) - CF(t = 6 \text{ days}))$.

ACPD
9, 23589–23622, 2009

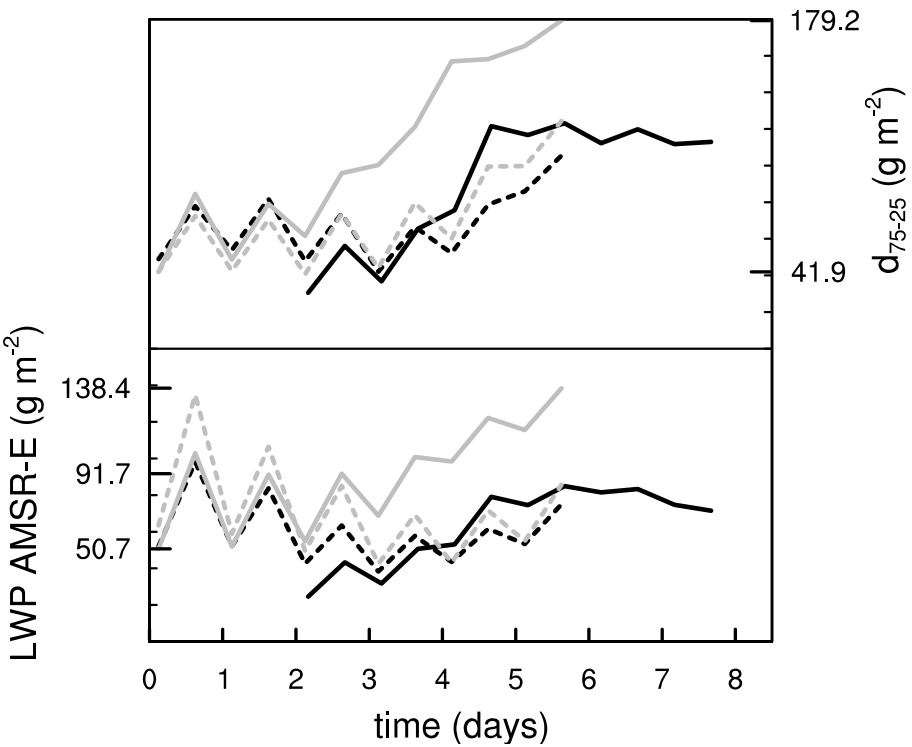

Fig. B1. AMSR-E LWP along the trajectories for the sets of trajectories analyzed in NEA (full black), NEP (full grey), SEA (dashed black) and SEP (dashed grey). Plotting conventions follow those in Fig. 2.

ACPD
9, 23589–23622, 2009